Systematic characterization of a PBI/H$_3$PO$_4$ sol–gel membrane—Modeling and simulation

C. Siegel [a,b,*], G. Bandlamudi [a,b], A. Heinzel [a,b]

[a] University of Duisburg-Essen, Institut für Energie- und Umweltverfahrenstechnik, Lotharstr. 1, D-47048 Duisburg, Germany
[b] Zentrum für BrennstoffzellenTechnik (ZBT) GmbH (Centre for Fuel Cell Technology), Carl-Benz-Str. 201, D-47057 Duisburg, Germany

ARTICLE INFO

ABSTRACT

This work presents a three-dimensional, steady-state, non-isothermal model of a high-temperature polymer-electrolyte-membrane fuel cell (HTPEMFC) using a phosphoric acid-doped polybenzimidazole (PBI/H$_3$PO$_4$) sol–gel membrane. The model accounts for the gold-plated copper current collector plates, the bipolar plates, all gas flow channels (flow-field), the gas diffusion layers, the reaction layers, and the membrane. Electrochemical reactions are modeled using an agglomerate approach and include the gas diffusivity and the gas solubility. The conductivity of the membrane is modeled using the Arrhenius equation to describe the temperature dependence. Finite elements are used to discretize all computational subdomains, and a commercially available code is used to solve the problem. The predicted values are compared to typical operating conditions, and a good agreement is found. The current density, the solid- and fluid-(gas)-phase temperatures and other quantities are analyzed throughout the computational subdomains. It was observed that the Arrhenius approach is valid in a certain temperature range and may overpredict the PBI/H$_3$PO$_4$ sol–gel membrane conductivity at higher solid-phase temperatures. Moreover, it is shown how the fluid-(gas)-phase temperature influences the solid-phase temperature and the current density distribution. Concrete values are deduced from the simulations and discussed according to experimental test.

1. Introduction

Within the last four decades, tremendous effort has been invested in both theoretical and experimental investigations of low-temperature polymer-electrolyte-membrane fuel cells (LTPEMFC). Based on phosphoric acid fuel cell (PAFC) technology, the HTPEMFC was presented as an interesting alternative in applications such as small stationary power plants (combined heat and power, CHP or μCHP) and power trains. Because of the benefits of using higher operating temperatures (e.g., 160–180 °C), this technology may play a significant role in new fuel cell systems because carbon monoxide (CO)-rich gases in the range of several percentages can be directly fed into the cell.

The possibility of using a PBI/H$_3$PO$_4$ system as a proton conductor in fuel cells was introduced by Wainright et al. [1], Samms et al. [2], and Wang et al. [3], among others. They tested polybenzimidazole films doped with phosphoric acid (PBI/H$_3$PO$_4$) as potential polymer electrolytes for fuel cell applications under various oper-

ating conditions. Since then, the physiochemical properties, water uptake, conductivity mechanisms and membrane performance has been studied by several groups [4–7]. Xiao et al. [8] presented sol–gel membranes with high levels of phosphoric acid, high conductivities, and acceptable mechanical properties at elevated temperatures. To date, only a few publications have investigated the short- and long-term behavioral patterns of commercially available HTPEM membrane-electrode-assemblies (MEAs). Schmidt [9] summarized HTPEMFC durability and degradation using a Celtec®-P Series 1000 MEA. The properties of this product running in start/stop operation mode were discussed in [10]. Electrochemical impedance spectroscopy (EIS) was used by Jalani et al. [11] to obtain a detailed view of PBI/H$_3$PO$_4$ sol–gel membrane processes under different operating conditions. They also highlighted the use of oxygen as cathode gas instead of air. In [12], Zhang et al. used EIS, cyclic voltammetry (CV) and fuel cell performance simulations to obtain the exchange current densities and activation energies for both half cell reactions. Moreover, they proposed different methods to improve gas diffusion processes. Zhang et al. [13] and Li et al. [14] summarized the current status of HTPEMFC research and development and described the advantages and challenges of operating a fuel cell at high temperatures.

Only a handful of publications concerning HTPEMFC modeling are currently available. Cheddie et al. [15–18] published one-,

* Corresponding author at: Zentrum für BrennstoffzellenTechnik (ZBT) GmbH (Centre for Fuel Cell Technology), Carl-Benz-Str. 201, D-47057 Duisburg, Germany. Tel.: +49 203 7598 1172; fax: +49 203 7598 2222.
E-mail address: c.siegel@zbt-duisburg.de (C. Siegel).

Nomenclature

a	surface area (m^2); activity
c	concentration (mol m^{-3})
C_p	heat capacity (J kg^{-1} K^{-1})
d	average hopping distance (m)
D	diffusion coefficient (m^2 s^{-1})
E	potential (V)
ΔE	activation energy (J mol^{-1})
f	ratio factor
F	Faraday constant (A s mol^{-1})
h	heat transfer coefficient (W m^{-3} K^{-1}) (W m^{-2} K^{-1})
H	solubility (mol m^{-3} atm^{-1}) (mol m^{-3} Pa^{-1}) (mol m^{-3} bar^{-1})
i	current density (A m^{-2})
j	current density (volumetric) (A m^{-3})
I	identity
k	thermal conductivity (W m^{-1} K^{-1}); constant
k_p	permeability (m^2)
K	used in Eqs. (7) and (8)
l	thickness (m)
m	loading (kg m^{-2}); mass fraction
M	molar mass (kg mol^{-1})
P	pressure (Pa)
r	radius (m)
R	gas constant (J mol^{-1} K^{-1})
S	general source/sink term (kg m^{-3} s^{-1}) (A m^{-3}) (W m^{-3})
ΔS	entropy (J mol^{-1} K^{-1})
T	phase temperature (°C) (K)
u	velocity vector (m s^{-1})
x	mole fraction; dimension in x-direction (m)
X	membrane doping level
y	dimension in y-direction (m)
z	dimension in z-direction (m); charge number

Greek letters

α	transfer coefficient; reciprocal of the number of all possible hopping directions
ε	porosity
ϕ	phase potential (V)
η	dynamic viscosity (Pa s); overpotential (V)
ν	factor in error estimation; diffusive volume (m^3 mol^{-1})
ν_0	hopping frequency
ρ	density (kg m^{-3})
σ	conductivity (S m^{-1}); pre-exponential factor (S K m^{-1}) (S K cm^{-1})
ω	mass fraction

Superscripts

0	void, reference
a	activation
eff	effective
f	formation
in	inlet
OCV	open circuit voltage
S	solid fraction in GDL
T	transposed

Subscripts

agg	agglomerate
a	anode-side
BPP	bipolar plate
c	cathode-side
C	carbon
Cu	copper
f	fluid-phase
GDL	gas diffusion layer
H$_2$	hydrogen
H$_2$O	water
H$_3$PO$_4$	phosphoric acid
i	index
j	index
m	membrane phase
O$_2$	oxygen
PBI	polybenzimidazole
PBI/(X − 2)H$_3$PO$_4$	PBI/amorphous phase H$_3$PO$_4$
Pt	platinum
Pt/C	platinum to carbon ratio
RL	reaction layer
s	solid-phase
T_s/T_f	solid to fluid heat transfer

two-, and three-dimensional models accounting for different operating conditions, membrane and reaction layer properties, layout optimization, and gas solubility and gaseous dissolution into the aqueous phase. Steady-state and transient three-dimensional HTPEMFC models have been presented by Peng et al. [19,20]. They showed that thermal management strongly affects the fuel cell performance and discussed key optimization parameters for performance improvements. Scott et al. [21] devised a one-dimensional model. The model was able to satisfactorily predict the polarization curve and was used to simulate the effects of catalyst loading and the Pt/C-ratio on fuel cell performance. Ubong et al. [22] developed a single-channel three-dimensional model in which the reaction layer was assumed to be infinitely thin, and the electrochemical reactions were described using an agglomerate approach. A complete three-dimensional model was developed and solved in [23], highlighting reaction-layer kinetics. Shamardina et al. [24] presented a simple and quickly solvable steady-state, isothermal, pseudo-two-dimensional model that accounted for crossover effects. Another analytical HTPEMFC model, published by Kulikovsky et al. [25], discussed important basic kinetic and transport parameters. A two-dimensional isothermal model was presented by Sousa et al. [26]. They treated the reaction layer as spherical catalyst agglomerates with porous inter-agglomerate spaces. The model was used to study the influence of the reaction layer properties on cell performance. A control-oriented, one-dimensional model was presented in [27], addressing the transient responses of HTPEMFC. Wang et al. [28] investigated the transient evolution of the carbon monoxide poisoning effect of PBI membrane fuel cells using a one-dimensional model. Another work that deals with CO poisoning and its dynamics is presented in [29]. Different HTPEMFC models were presented in [30–32], mainly addressed solid- and fluid-(gas)-phase temperature and PBI/H$_3$PO$_4$ sol–gel membrane behavior. Structural mechanics, namely localized fluid-structural interactions (LSFI), were also analyzed [33].

The current state-of-the-art HTPEMFC technology offers significant optimization potential. Besides material demands, operating schemes are of great importance in ensuring effective and efficient fuel cell operation, decreasing degradation, and reaching long operating times. HTPEMFC modeling and simulation may help achieve these goals faster. This work presents a general-purpose, large-scale HTPEMFC model focusing on the behavior of various quantities under given operating conditions. The simulated current density and fluid-flow distribution should help to optimize

Table 1
Spatial dimensions (HTPEMFC assembly/computational subdomains) and MEA data [34].

Symbol	Value	Unit	Note	Reference
l_{Cu}	0.001	m	Thickness	
l_{BPP}	0.005	m	Thickness	
l_{GDL}	400×10^{-6}	m	Thickness (uncompressed)	
$l_{RL,a}$	30×10^{-6}	m	Thickness (anode side)	
$l_{RL,c}$	40×10^{-6}	m	Thickness (cathode side)	
l_{MEM}	152×10^{-6}	m	Thickness (uncompressed)	
a_{MEA}	0.005	m^2	MEA active surface area	
X	32		PBI/H_3PO_4 doping level	[8]
$m_{Pt,a}$	0.01	kg m^{-2}	Anode-side platinum loading	[9,10]
$m_{Pt,c}$	0.0075	kg m^{-2}	Cathode-side platinum loading	[9,10]
$f_{Pt/C,a}$	0.3		Anode-side Pt/C ratio	
$f_{Pt/C,c}$	0.3		Cathode-side Pt/C ratio	

the gas flow channel design for HTPEMFC applications. As for the energy transport, different source term contributions are calculated. Results are compared to experimental tests to make this work complete. Solver settings, soft-, and hardware requirements are reported in great detail.

The work in [34] is summarized below. Theoretical derivations and experimental investigations were performed using a HTPEMFC. Further, the electrochemical behavior was highlighted. The maximum theoretical thermodynamic potential and maximum theoretical cell efficiency was calculated using thermodynamics and compared to the values of a LTPEMFC. Next, a complete cell assembly (same as in Fig. 2) was analyzed using EIS to deduce assembly resistance contributions, followed by voltage loss estimations. The last section elucidated conductivity measurements and theoretical calculations on the PBI/H_3PO_4 sol–gel membrane composition (BASF Celtec®-P Series 2000 MEA). Some modeling parameters pertinent to HTPEMFCs are directly taken from [34] and serve as a basis for modeling and simulation (see Tables 1–3).

2. Modeling aspects

2.1. Model geometry

The three-dimensional model geometry used for all computations is given in Fig. 1. It is an exact representation of the HTPEMFC assembly that was used for all experimental tests, as described in [34], and includes gold-plated copper current collectors (Cu) and four high-temperature stable bipolar plates (BPP). The gas flow channels are machined into the graphite (six channel parallel serpentine flow-field with a channel-to-land ratio of 1.0/1.0 (1×10^{-3} m/1×10^{-3} m)). The gas flow channel depth is 1×10^{-3} m (z-coordinate). The MEA is sandwiched between the BPPs and includes the gas diffusion layers (GDL), the reaction layers (RL), and a PBI/H_3PO_4 sol–gel membrane (BASF Celtec®-P Series 2000 MEA). The exact spatial dimensions of the components can be found in Table 1.

2.2. Transport equations

2.2.1. Momentum transport

The continuity equation and the incompressible Navier–Stokes equations (density assumed to be constant or nearly constant) are solved to account for the laminar gas flow and pressure distribution within the anode- and cathode-side gas flow channels. Eq. (1) accounts for advection momentum flux and momentum imparted due to pressure and viscosity.

$$\nabla \cdot u = 0$$
$$\rho \cdot (u \cdot \nabla) \cdot u = \nabla \cdot (-P \cdot I + \eta \cdot (\nabla u + (\nabla u)^T)) \tag{1}$$

The Brinkman equations (2) describe the gas flow within porous media, i.e., GDL and RL. This mathematical model extends Darcy's

law to include a term that accounts for the viscous transport in the momentum balance, and it treats both the pressure and the flow-velocity vector as independent variables.

$$\nabla \cdot u = \frac{S_m}{\rho}$$
$$\left(\frac{\eta}{k_p} + S_m\right) \cdot u = \nabla \cdot \left(-P \cdot I + \frac{1}{\varepsilon} \cdot \left(\eta \cdot (\nabla u + (\nabla u)^T) - \left(\frac{2}{3} \cdot \eta\right) \cdot (\nabla \cdot u) \cdot I\right)\right) \tag{2}$$

In Eqs. (1) and (2), u is the velocity vector, and P the pressure.

2.2.2. Mass (species) transport

The gas flow is predominantly convective in the gas flow channels, whereas it is predominantly diffusive within the porous media. Mass (species) transport is solved using Stefan-Maxwell diffusion in the convection application mode accounting for hydrogen (H_2) and water (H_2O) at the anode and oxygen (O_2), H_2O, and nitrogen (N_2) at the cathode (3). The reaction rates appear as source/sink terms S_ω. Note that the amount of water in both gas streams at the inlets is small. This is implied by our laboratory hardware, but it should not be neglected.

$$\nabla \cdot \left(\rho \cdot \omega_i \cdot u - \rho \cdot \omega_i \cdot \sum_{j=1}^{n} \tilde{D}_{ij}^{eff} \cdot \left(\nabla x_j + (x_j - \omega_j) \cdot \frac{\nabla P}{P}\right)\right) = S_{\omega_i} \tag{3}$$

2.2.3. Charge transport

Two Poisson equations are used to evaluate charge transport (4). The solid-phase potential (subscript s) distribution is solved within the gold-plated copper current collectors, the BPPs, GDL, and the RL. The membrane-phase potential (subscript m) is solved within the RL in the membrane. Both equations are coupled through their current source/sink terms.

$$-\nabla \cdot (\sigma_s \cdot \nabla \phi_s) = -S_\phi$$
$$-\nabla \cdot (\sigma_m \cdot \nabla \phi_m) = +S_\phi \tag{4}$$

2.2.4. Energy transport

The thermal behavior is described using a two-equation system (5), separately accounting for the solid-phase (T_s) and the fluid-(gas)-phase temperatures (T_f), as introduced by our group in 2007 for HTPEMFC models [30,31]. This is necessary because of the large temperature difference between the feed-gas temperature (fluid-(gas)-phase) and the cell-operating temperature (solid-phase) and represents the thermal interactions between the two phases. This behavior was confirmed by performing segmented temperature measurements. The solid-phase temperature distribution is calculated for the gold-plated copper current collectors, the BPPs, the solid matrix of the porous media and the membrane. The fluid-(gas)-phase temperature distribution is solved within the gas flow channel and within the porous media. Both equations are coupled through their source/sink terms and account for possible heat
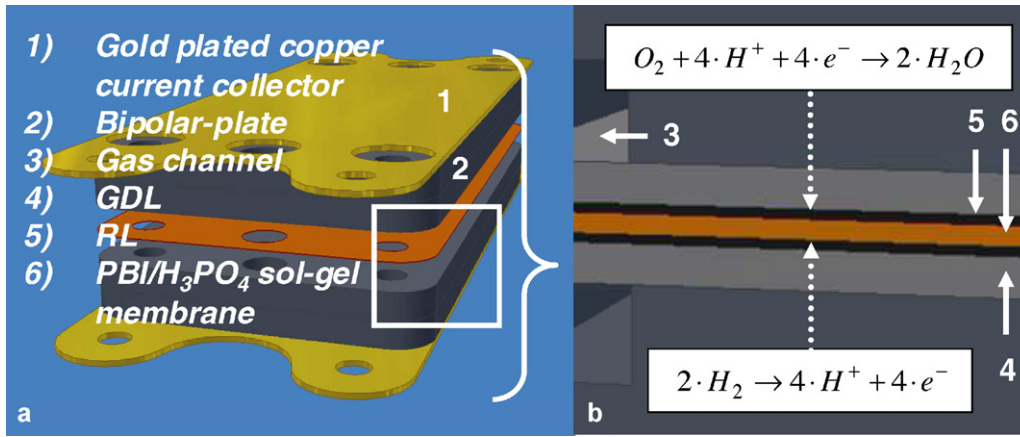
Fig. 1. (a) CAD representation of the HTPEMFC assembly; (b) detailed view of the MEA and electrochemical reactions.

transfer between the solid- and the fluid-(gas)-phase using a volumetric (intrinsic) heat transfer coefficient (h_{T_s}/T_f). In general, this coefficient is a function of the morphology of the porous media. As stated in [35], typical values for metal foams vary from 2×10^4 to $2 \times 10^5 \, \text{W m}^{-3} \, \text{K}^{-1}$ for a porosity between 0.7 and 0.95. In this work, a similar value is used.

$$\nabla \cdot (-k \cdot \nabla T_s) = S_{T_s}$$
$$\nabla \cdot (-k \cdot \nabla T_f) = S_{T_f} - \rho \cdot C_p \cdot u \cdot \nabla T_f \tag{5}$$

2.3. Source/sink term couplings

Mass transport source/sink terms are non-zero only in the RL subdomains. The reaction rates for H_2, O_2, and H_2O are described with Eq. (6).

$$S_{\omega_i} = \begin{cases} -j_a \cdot \dfrac{M_{H_2}}{2 \cdot F} \\ j_c \cdot \dfrac{M_{O_2}}{4 \cdot F} \\ -j_c \cdot \dfrac{M_{H_2O}}{2 \cdot F} \end{cases} \tag{6}$$

Agglomerate structure models have been developed to describe LTPEMFC and PAFC behavior, among others [36]. In this work, an agglomerate model is used to simulate electrochemical half-cell reactions. The LTPEMFC model from COMSOL Multiphysics® [37] and the equations presented in [38] serve as a foundation and are adopted for HTPEMFC modeling and simulation by accounting for gas diffusivity and gas solubility in H_3PO_4, and the amorphous phase of H_3PO_4, respectively. It is referred to [39] for a detailed description of the analytical solution of a diffusion reaction problem in a spherical porous particle. In this work, the reactions are assumed to occur in electrolyte-filled agglomerate zones. These zones contain channels of the amorphous phase H_3PO_4 into which the gases dissolve. Gas-transport limitations of diffusion processes in the agglomerates are characterized by an effectiveness factor and the Thiele modulus (dimensionless group). The characteristic length scale is the radius of the agglomerate r_{agg}. Eq. (7) describes the volumetric current density at the anode.

The transfer coefficients α_a and α_c in Eqs. (7) and (8) depend on many parameters, including temperature. In this work, at the anode-side, a well-recognized value of 0.5 was assumed, see e.g. [26]. At the cathode-side, the reported values vary within a certain range. In [26], a value of 0.73 best described the behavior of the base system. Huang et al. [41] reported a value of 0.67 at 150 °C for O_2 reduction on Pt in 85% H_3PO_4. Kulikovsky et al. [25] discussed the Tafel slope and used a value of 0.777 for the transfer coefficient. In this work, a cathode-side transfer coefficient of 0.89 returned the best results.

As for solid-phase energy transport, the source/sink terms are given in Eq. (9) and account for ohmic and/or protonic heating (membrane heating), irreversible reaction heat, and reaction entropy for the following subdomains: the gold-plated copper current collector and bipolar plates, GDL, anode-side RL, cathode-side RL, and the membrane (top to bottom).

$$S_{T_s} = \begin{cases} \dfrac{i_s^2}{\sigma_s} \\ \dfrac{i_s^2}{\sigma_s} - h_{T_s/T_f} \cdot (T_s - T_f) \\ \dfrac{i_s^2}{\sigma_s} + \dfrac{i_m^2}{\sigma_m} + j_a \cdot \eta_a - h_{T_s/T_f} \cdot (T_s - T_f) \\ \dfrac{i_s^2}{\sigma_s} + \dfrac{i_m^2}{\sigma_m} + j_c \cdot \eta_c + j_c \cdot \dfrac{\Delta S_c \cdot T_s}{4 \cdot F} - h_{T_s/T_f} \cdot (T_s - T_f) \\ \dfrac{i_m^2}{\sigma_m} \end{cases} \tag{9}$$

Eq. (10) introduces the heat source/sink term for the fluid-(gas)-phase temperature within the GDL and RL subdomains.

$$S_{T_f} = h_{T_s/T_f} \cdot (T_s - T_f) \tag{10}$$

2.4. PBI/H₃PO₄ sol–gel membrane modeling

The following equations describe the behavior of a highly doped PBI/H_3PO_4 system of approximately 30–35 mol of H_3PO_4 per PBI repeat unit. As mentioned in [34], the properties of the membrane are significantly affected by the polymer molecular structure and

$$j_a = -(1 - \varepsilon_{RL}^0) \cdot 3 \cdot 2 \cdot F \cdot D_{H_2, PBI/(X-2)H_3PO_4} / r_{agg}^2 \cdot \left(c_{H_2, PBI/(X-2)H_3PO_4} - c_{H_2}^{in} \cdot e^{\alpha_a \cdot F/R \cdot T_f \cdot \eta_a} \right) \cdot (1 - K_a \cdot \coth(K_a))$$
$$K_a = \sqrt{i_{PBI/(X-2)H_3PO_4, a}^0 \cdot a_a \cdot 1/2 \cdot F \cdot c_{H_2}^{in} \cdot D_{H_2, PBI/(X-2)H_3PO_4}} \cdot r_{agg} \tag{7}$$

The cathode volumetric current density is described using Eq. (8).

$$j_c = (1 - \varepsilon_{RL}^0) \cdot 3 \cdot 4 \cdot F \cdot D_{O_2, PBI/(X-2)H_3PO_4} / r_{agg}^2 \cdot c_{O_2, PBI/(X-2)H_3PO_4} \cdot (1 - K_c \cdot \coth(K_c))$$
$$K_c = \sqrt{i_{PBI/(X-2)H_3PO_4, c}^0 \cdot a_c \cdot 1/4 \cdot F \cdot c_{O_2}^{in} \cdot D_{O_2, PBI/(X-2)H_3PO_4} \cdot e^{-\alpha_c \cdot F/R \cdot T_f \cdot \eta_c}} \cdot r_{agg} \tag{8}$$

the preparation process itself. Because two H_3PO_4 molecules are bonded to PBI, $X-2$ molecules remain free and tend to form an amorphous phase within the PBI/H_3PO_4 sol–gel membrane [7]. It is expected that the final membrane initially consists of more than 85 wt.% H_3PO_4. The amorphous phase H_3PO_4 volume fraction $\varepsilon_{PBI/(X-2)H_3PO_4}$ within the membrane is calculated using Eq. (11).

$$\varepsilon_{PBI/(X-2)H_3PO_4} = \left(\frac{M_{PBI}/M_{H_3PO_4} + X}{X-2} \right)^{-1} \tag{11}$$

It is accepted that the amorphous phase H_3PO_4 volume fraction contributes to the high membrane conductivity via a Grotthuss proton switching mechanism. The strong temperature dependency of the membrane conductivity can be described using an Arrhenius approach [7].

$$\sigma = \sigma_0(k_i, X)/T_s \cdot e^{(-\Delta E^a(k_i,X)/R \cdot T_s)} \tag{12}$$

The pre-exponential term σ_0 is assumed to be independent of the cell operating temperature and decreases with higher doping levels X. The concentration of the mobile species in Eq. (13) should change with the doping level [7].

$$\sigma_0 = \left(\frac{z^2 \cdot F^2}{R} \right) \cdot \alpha \cdot \upsilon_0 \cdot d^2 \cdot c \cdot e^{\Delta S + \Delta S^f/R} \tag{13}$$

The activation energy of the conductivity depends on multiple factors, including the membrane doping level and the polymer backbone structure. Only minor amounts of valuable data are available in the literature for PBI/H_3PO_4 sol–gel membranes [11,12]. In this work, the obtained values for the activation energy and pre-exponential factor are taken from [34].

2.5. Additional modeling equations

In [40], it was demonstrated that the logarithmic exchange current density of oxygen reduction at platinum-interfaced PBI/H_3PO_4 linearly increases with the amorphous phase H_3PO_4 volume fraction. From this data, the authors of that report estimated the exchange current density for concentrated H_3PO_4 and reported consistent values. In this work, Eq. (14) is used to calculate the cathode-side exchange current density $i^0_{PBI/(X-2)H_3PO_4,c}$.

$$i^0_{PBI/(X-2)H_3PO_4,c} = i^0_{H_3PO_4,c} \cdot \frac{1}{10^{4.16 \cdot (1-\varepsilon_{PBI/(X-2)H_3PO_4})}} \tag{14}$$

In [41], it was found that the linearity of the logarithmic current density and the reciprocal temperature plot indicates Arrhenius behavior with an apparent activation energy of 41840 J mol^{-1} (85 wt.% H_3PO_4). Reported values are in the range of 0.01–0.02 A m^{-2} for typical operating temperatures. In the present work, the exchange current density for concentrated H_3PO_4 $i^0_{H_3PO_4,c}$ is calculated with Eq. (15). A factor of 1×10^4 is used to convert into SI units (A m^{-2}).

$$i^0_{H_3PO_4,c} = 1 \times 10^4 \times 10^{(-0.491-2193 \cdot 1/T_f)} \tag{15}$$

For the anode half-cell reaction, the exchange current density is taken to be 1×10^8 times the cathode-side exchange current density, a value that is consistent with many other published works, see e.g. [18]. The effective surface area of the RL (16) is a function of the catalyst surface area per unit mass of the catalyst particle, the platinum loading, and the thickness of the RL [42].

$$a_i = a_{Pt,i} \cdot \frac{m_{Pt,i}}{l_{RL,i}} \tag{16}$$

Gallart [43] summarized the available catalyst surface area per unit mass of the catalyst particle data and coupled it to the platinum-

Table 2
Modeling constants and parameters.

Symbol	Value	Unit	Reference
ΔE^a	18,484	J mol^{-1}	[34]
F	96,485	A s mol^{-1}	
$h_{BPP/CH,a}$	15	W m^{-2} K^{-1}	
$h_{BPP/CH,c}$	40	W^{-2} K^{-1}	
h_{T_s/T_f}	1×10^5	W m^{-3} K^{-1}	[41]
k	3.16×10^{-8}		
k_{Cu}	400	W m^{-1} K^{-1}	[37]
k_{BPP}	20	W m^{-1} K^{-1}	
$k_{GDL,x,y}$	2.5	W m^{-1} K^{-1}	
$k_{GDL,z}$	0.25	W m^{-1} K^{-1}	
$k_{p,GDL}$	5×10^{-13}	m^2	
$k_{p,RL}$	1×10^{-13}	m^2	
k_{PBI}	0.45	W m^{-1} K^{-1}	
k_{RL}	0.3	W m^{-1} K^{-1}	
M_{H_2}	0.002	kg mol^{-1}	
M_{O_2}	0.032	kg mol^{-1}	
M_{N_2}	0.028	kg mol^{-1}	
M_{H_2O}	0.018	kg mol^{-1}	
$M_{H_3PO_4}$	0.098	kg mol^{-1}	
M_{PBI}	0.308	kg mol^{-1}	
r_{agg}	1×10^{-9}	m	[43]
R	8.314	J mol^{-1} K^{-1}	
α_a	0.5		
α_c	0.89		
ε^0_{GDL}	0.78 (uncompressed)		
$\ln(\sigma_0 \cdot T_s)$	9.5211	S K cm^{-1}	[34]
σ_{Cu}	1×10^4	S m^{-1}	[37]
σ_{BPP}	3600	S m^{-1}	
$\sigma_{GDL,x,y,z}$	220	S m^{-1}	[40]
$\sigma_{s,RL}$	450	S m^{-1}	[38]
$\sigma_{m,RL}$	13	S m^{-1}	[38]
υ_{H_2}	7.07×10^{-6}	m^3 mol^{-1}	
υ_{O_2}	16.6×10^{-6}	m^3 mol^{-1}	
υ_{N_2}	17.9×10^{-6}	m^3 mol^{-1}	
υ_{H_2O}	12.7×10^{-6}	m^3 mol^{-1}	
ρ_C	2000	kg m^{-3}	[37]
$\rho_{PBI/(X-2)H_3PO_4}$	1698	kg m^{-3}	[40]
ρ_{Pt}	21,500	kg m^{-3}	[37]

to-carbon ratio, as shown in Eq. (17).

$$a_{Pt,i} = 7.401 \times 10^5 \cdot f^4_{Pt/C,i} - 1.811 \times 10^6 \cdot f^3_{Pt/C,i} + 1.545 \times 10^6 \cdot f^2_{Pt/C,i}$$
$$- 6.453 \times 10^5 \cdot f_{Pt/C,i} + 2.054 \times 10^5 \tag{17}$$

The local RL overpotential η_i is defined as the difference between the solid- and membrane-phase potentials. This potential difference drives the cell current, keeping the electrochemical half-cell reactions continuous. It is calculated with Eqs. (18) and (19).

$$\eta_a = \phi_s - \phi_m - 0 \tag{18}$$
$$\eta_c = \phi_s - \phi_m - E^{OCV} \tag{19}$$

The maximum equilibrium potential with respect to temperature and partial pressures is calculated using the Nernst equation, as discussed in [34] for a HTPEMFC.

Accounting for gas diffusivity and solubility in the electrolyte is crucial for HTPEMFC modeling, as mentioned in the few currently available studies [18,26,40]. In [40], the authors found that the oxygen diffusivity increases with increasing PBI/$(X-2)H_3PO_4$ and that it does not significantly vary from the data available for hot concentrated H_3PO_4. In the present work, a similar expression is used, as presented in [18]. A Bruggeman relation with an exponent of 1.8 is used to account for the agglomerate structure (20) [40].

$$D_{O_2,PBI/(X-2)H_3PO_4} = D_{O_2,H_3PO_4} \cdot (\varepsilon_{PBI/(X-2)H_3PO_4} \cdot \varepsilon^0_{RL})^{1.8} \tag{20}$$

The oxygen solubility is generally higher (about four times higher than expected for pure H_3PO_4 under given conditions [14]) than the values reported for hot concentrated H_3PO_4. In [40], the authors stated that these higher values must be related to the presence of

PBI. Cheddie and Munroe [18] related the values of hot concentrated H_3PO_4 to the values presented by Liu et al. [40] using Eq. (21).

$$H_{O_2, PBI/(X-2)H_3PO_4} = \varepsilon_{PBI/(X-2)H_3PO_4}^{1.945} \cdot ((H_{O_2, H_3PO_4})$$
$$+ 5.79 \cdot (1 - \varepsilon_{PBI/(X-2)H_3PO_4}^{1.8})) \tag{21}$$

Data for the hydrogen oxidation reaction at the anode-side are not readily available, so the hydrogen diffusivity is taken to be two times the oxygen diffusivity and the hydrogen solubility is taken to be approximately four times the oxygen solubility. The same behavior is assumed as in a water system [18]. On the other hand, one has to note that Li et al. [14] reported solubility values of 1.6×10^{-5} mol cm^{-3} bar^{-1} for hydrogen and 1.9×10^{-5} mol cm^{-3} bar^{-1} for oxygen in PBI membranes.

$$D_{H_2, PBI/(X-2)H_3PO_4} = 2 \cdot D_{O_2, PBI/(X-2)H_3PO_4} \tag{22}$$

$$H_{H_2, PBI/(X-2)H_3PO_4} = 4.44 \cdot H_{O_2, PBI/(X-2)H_3PO_4} \tag{23}$$

The gas diffusion coefficient and gas solubility in the amorphous phase H_3PO_4 must also be related to the reported values for hot concentrated H_3PO_4. Klinedinst et al. [44] highlighted that oxygen diffusivity and solubility in hot concentrated H_3PO_4 exhibit exponential reciprocal temperature dependencies over sufficiently small temperature ranges. The activation energy for oxygen diffusion and the enthalpy of the solution vary with concentration. In this work, the transport properties of oxygen in concentrated H_3PO_4 are related to the temperature and the acid concentration, as presented in [18]. Similar empirical equations were used in [26].

$$D_{O_2, H_3PO_4} = 1 \times 10^{-9} \cdot e^{((-192.55 \cdot m_{H_3PO_4}^2 + 323.55 \cdot m_{H_3PO_4} - 125.61) + 62010 \cdot m_{H_3PO_4}^2 - 105503 \cdot m_{H_3PO_4} + 40929/T_f)} \tag{24}$$

$$H_{O_2, H_3PO_4} = 1 \times 10^{-1} \cdot e^{((257.13 \cdot m_{H_3PO_4}^2 - 431.08 \cdot m_{H_3PO_4} + 178.45) + -93500 \cdot m_{H_3PO_4}^2 + 156646 \cdot m_{H_3PO_4} - 64288/T_f)} \tag{25}$$

The H_3PO_4 concentration within the MEA is expected to change during cell operation (compare with Fig. 13). In [42], a correlating equation for H_3PO_4 vapor pressure is given (80–101 wt.% acid in the range of 130–170 °C). From their experimental data, Souza et al. [26] generated an equation that coupled concentration and water vapor partial pressure (26).

$$x_{H_3PO_4} = \frac{\ln(x_{H_2O} \cdot P) + 2765.1/T_f - 22.002}{-4121.9/T_f + 2.5929} \tag{26}$$

A similar equation was used by Choudhury et al. [36] to correlate the H_3PO_4 concentration and equilibrium vapor pressure at a given temperature (equilibrium between the humidity and the H_3PO_4/H_2O solution). The mole fraction of H_3PO_4 is converted into mass fraction with Eq. (27), similar to [42].

$$m_{H_3PO_4} = \frac{136 \cdot x_{H_3PO_4}}{111 \cdot x_{H_3PO_4} + 25} \tag{27}$$

Finally, the hydrogen and oxygen agglomerate concentration is calculated using Henry's law (28) and (29), incorporating the partial pressures of hydrogen and oxygen (gas/electrolyte (amorphous phase H_3PO_4) interface). Note that different solubility units are used in the literature, e.g., mol m^{-3} atm^{-1}, mol m^{-3} Pa^{-1} or mol m^{-3} bar^{-1}.

$$c_{H_2, PBI/(X-2)H_3PO_4} = \frac{P \cdot x_{H_2}}{H_{H_2, PBI/(X-2)H_3PO_4}} \tag{28}$$

$$c_{O_2, PBI/(X-2)H_3PO_4} = \frac{P \cdot x_{O_2}}{H_{O_2, PBI/(X-2)H_3PO_4}} \tag{29}$$

Table 3
Base case operating parameters [34].

T_∞ (ambient) (°C)	21	
T_{cell} (solid-phase) (°C)	160	
	Anode side	Cathode side
Gas	Hydrogen	Air
Flow rate (l min^{-1})	Stoichiometry 1.35	Stoichiometry 2.5
Gas inlet temperature (°C)	21	21
Gas humidity (% rh)	0.2	2
Outlet pressure (Pa)	1.01325×10^5	1.01325×10^5

2.6. Solid- and fluid-(gas)-phase properties and material correlations

A woven-type GDL (similar to E-tek ELAT® products [45]) is considered herein. It consists of a void volume fraction (porosity; superscript 0) and a solid-phase volume fraction (subscript s), as indicated by Eq. (30).

$$\varepsilon_{GDL}^0 + \varepsilon_{GDL}^S = 1 \tag{30}$$

The RL structure is more complex. Different volume fractions are needed to calculate the effective RL properties, e.g., thermal, electrical or protonic conductivities. The volume fraction of platinum and carbon (subscript Pt/C) is calculated with Eq. (31), taking its thickness and the catalyst properties into account [46].

$$\varepsilon_{Pt/C} = \frac{m_{Pt}}{l_{RL} \cdot f_{Pt/C}} \cdot \left(\frac{f_{Pt/C}}{\rho_{Pt}} + \frac{1 - f_{Pt/C}}{\rho_C} \right) \tag{31}$$

In this model, the fraction of the volume occupied by the amorphous phase H_3PO_4 inside the agglomerate is calculated with Eq. (32) [46].

$$\varepsilon_{PBI/(X-2)H_3PO_4} = \frac{m_{Pt}}{l_{RL} \cdot f_{Pt/C}} \cdot \left(\frac{f_{PBI/(X-2)H_3PO_4}}{(1 - f_{PBI/(X-2)H_3PO_4}) \cdot \rho_{PBI/(X-2)H_3PO_4}} \right) \tag{32}$$

Finally, the RL porosity can be calculated with Eq. (33).

$$\varepsilon_{RL}^0 = 1 - \varepsilon_{Pt/C} - \varepsilon_{PBI/(X-2)H_3PO_4} \tag{33}$$

The binary diffusion coefficients $\tilde{D}_{ij}$ are calculated for all pairs of species in the fluid-(gas)-phase mixture using Eq. (34) and are known to vary with pressure and temperature.

$$\tilde{D}_{ij} = k \cdot \frac{T_f^{1.75}}{P \cdot (v_i^{1/3} + v_j^{1/3})^2} \cdot \sqrt{\frac{1}{M_i} + \frac{1}{M_j}} \tag{34}$$

The effective porous media binary diffusivities $\tilde{D}_{ij}^{eff}$ in Eq. (3) are calculated using the respective void volume fraction and a Bruggeman relationship with an exponent of 1.5, which is consistent with other works.

$$\tilde{D}_{ij}^{eff} = \tilde{D}_{ij} \cdot (\varepsilon_{GDL,RL}^0)^{1.5} \tag{35}$$

The densities of the fluid-(gas)-phase mixture within the gas flow channel and the porous media are calculated using the mole fraction and the molar mass of the gas species.

$$\rho_i = \sum_i x_i \cdot M_i \cdot \frac{P}{R \cdot T_f} \tag{36}$$

The fluid-(gas)-phase properties, namely the density, thermal conductivity, heat capacity and dynamic viscosity, are taken from the material library provided by the software used and depend on the fluid-(gas)-phase temperature.

The thermal conductivity of the membrane k_{MEM} is calculated using the thermal conductivities of PBI and amorphous phase H_3PO_4 (amorphous phase H_3PO_4 treated as concentrated H_3PO_4).

$$k_{MEM} = k_{PBI} \cdot (1 - \varepsilon_{PBI/(X-2)H_3PO_4}) + k_{PBI/(X-2)H_3PO_4} \cdot \varepsilon_{PBI/(X-2)H_3PO_4} \tag{37}$$

Based on the data provided by Turnbull [47], the thermal conductivity data is extrapolated for higher temperatures and H_3PO_4 concentrations with Eq. (38).

$$k_{PBI/(X-2)H_3PO_4} \approx k_{H_3PO_4} = \left(\frac{11.727 + 0.01864 \cdot T_s - 0.02169 \cdot c_{H_3PO_4} - 0.0000338 \cdot c_{H_3PO_4} \cdot T_s}{1 \cdot 10^4} \right) \cdot 418.68 \tag{38}$$

The remaining gas mixture properties were calculated using average-based mole or mass fractions. Other modeling parameters can be found in Table 2. Some of these values (or their orders of magnitude) were provided by their respective manufacturers.

2.7. Boundary conditions

Boundary conditions are crucial for accurate simulation results. They are precisely applied according to the experimental setup (Table 3). The gas composition (mass fractions), gas temperature, and gas velocity (mass flux) are chosen at the gas flow channel inlets. The inlet flow should be fully developed when entering the cell. An additional pressure variable (weak contribution/additional degrees of freedom (DOF)) is used to define a laminar inflow condition. Reference concentrations are deduced from the inlet conditions. At the outlets, pressure and convective flux boundary conditions are used. To conserve charge, the cell voltage is given and the current density calculated. The cell operating voltage is defined at the cathode-side gold-plated copper current collector. At the anode-side, the potential is fixed at zero. The cell operating temperature (solid-phase) is defined at the anode- and cathode-side gold-plated copper current collector boundaries. At the bipolar plate walls (gas flow channel walls), a no-slip boundary condition is defined for momentum transport, and a heat transfer coefficient is used to account for the heat by the absorbed gases in both energy transport equations. At all other internal boundaries, symmetry, continuity or insulation boundary conditions are used.

2.8. Assumptions and simplifications

The following assumptions and simplifications are used:

(1) Steady-state operating conditions.
(2) Continuity is prescribed at internal boundaries (interfaces); all contact resistances are neglected.
(3) Some material properties are assumed to be isotropic and macrohomogeneous, whereas others account for the different material properties in the x-, y-, and z-directions.
(4) A microporous layer and its influence on the quantities' behavior and distribution is not explicitly considered in this model.
(5) All product water is assumed to be vaporous because of the high operating temperature (no phase change) and to leave the cell assembly in vapor form.
(6) Gas and water crossover through (or water uptake by) the PBI/H_3PO_4 sol–gel membrane is neglected.
(7) The initial concentration of the amorphous phase H_3PO_4 volume fraction inside the RL and inside the membrane is assumed to be 85 wt.% at room temperature and pressure (RTP).
(8) The membrane is considered to be a system of PBI, H_3PO_4 and H_2O only (molecular H_3PO_4, other H_3PO_4 forms are neglected).
(9) Low velocities (low Reynolds numbers) are expected in the gas streams. Laminar inflow conditions can be assumed.
(10) All agglomerates are assumed to be geometrically identical, spherical in shape, and of the same radii. An additional H_3PO_4 (or water) film surrounding the agglomerate is not considered.
(11) There is no heat transfer towards the surroundings.
(12) There is no (partial) H_3PO_4 flooding of the GDL and no H_3PO_4 catalyst absorption

The listed assumptions are generally adopted when modeling a HTPEMFC (e.g., assumptions 2, 5, 9). Some of the simplifications are directly related to steady-state operating conditions (assumption 1), the modeling level, the purpose, and the outcome of the study (e.g., contact resistances are mostly neglected in similar studies but should be included when modeling cell compression, structural mechanics, and/or cell ageing). Other simplifications base on material properties and/or material casting methods (e.g., assumption 7). There is no doubt that assumptions 4, 6, 10, and 12 are the major drawbacks of this model setup and should be updated in future works. Assumption 6 is used since the model deals with steady-state operating conditions, high operating temperatures and low vapor pressure. Start-up and shut-down periods are not investigated. Assumption 11 is discussed in more detail in Section 5.4.

Based on the simulation results and the observations made during experimental test, it can fairly be concluded that all assumptions are acceptable when focusing complete 3D cell level modeling and simulation.

3. HTPEMFC operation

The reference HTPEMFC in Fig. 2 includes a commercially available PBI/H_3PO_4 sol–gel membrane (Celtec®-P Series 2000 MEA) that is stable at high temperatures. The available MEA data can be found in Table 1. The HTPEMFC assembly was temperature-controlled using heating elements. After steady state operating conditions were achieved, a defined amount of hydrogen and air was fed in a counter-flow configuration using mass flow controllers. The solid- and fluid-(gas)-phase temperature was measured close to the inlets and outlets. Additionally, the pressure and relative humidity was monitored at the in- and outlets.

Hydrogen at the anode-side and air at the cathode-side pass the gas flow channels (flow-field) and partially diffuse through the porous media towards the RL, in which the electrochemical half-cell reactions take place according to the equations given in Fig. 1. The resulting voltage of a single fuel cell is in the order of 1 V. Power can be drawn using an external load connected to both gold-plated copper current collectors. Moreover, water and heat is produced by the exothermic reactions.

4. Computational aspects

4.1. Software and hardware

The model geometry was created using CAD software and imported as a neutral standard (*.iges) into commercially available FEM/CFD-software COMSOL Multiphysics® v3.5a (64 bit version) running on a PC (double quadcore with 64 GB RAM). Next, the com-
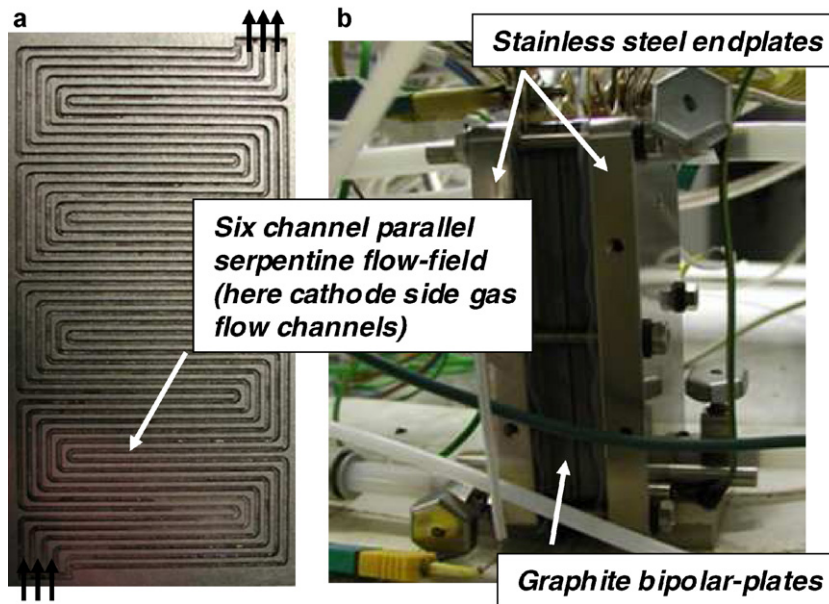
Fig. 2. (a) Gas flow channels; (b) HTPEMFC assembly used for all experimental tests.

plete 3D geometry was discretized using 355,431 tetrahedral and 397,644 prism elements (Fig. 3). Meshing needed to be performed carefully to minimize the number of DOF and therefore the memory requirements. However, the quality of the mesh was crucial for accurate (mesh-independent) simulation results. The membrane subdomain was only meshed with tetrahedral elements because both bipolar plates (and flow-fields) are turned 180° against each other. This results in a different boundary mesh at both membrane/RL interfaces. The mesh of the porous media subdomains was refined to account for the expected local quantity gradients, whereas a coarser mesh was used within the gold-plated copper current collector and BPP subdomains (only scalar variables had to be solved within these subdomains). The total number of DOF for this problem was 12,665,886.

4.2. Solution procedure and convergence behavior

Solving a large scale fuel cell model using finite elements is not easy. A large amount of memory is needed, even when using iterative solvers (compare with Table 4). Additionally, one has to carefully tune these solvers to reach a converged solution. The best possible initial conditions were generated using a series of parametric dummy simulations. The problem was solved using the chemical engineering and heat transfer modules provided by the software. The solution procedure was rather complex due to the strong multiphysical couplings of all transport equations, as explained in [48]. The complete Navier–Stokes equations were solved first, followed by the charge and mass (species) transport equations and, finally, the solid- and fluid-(gas)-phase tempera-
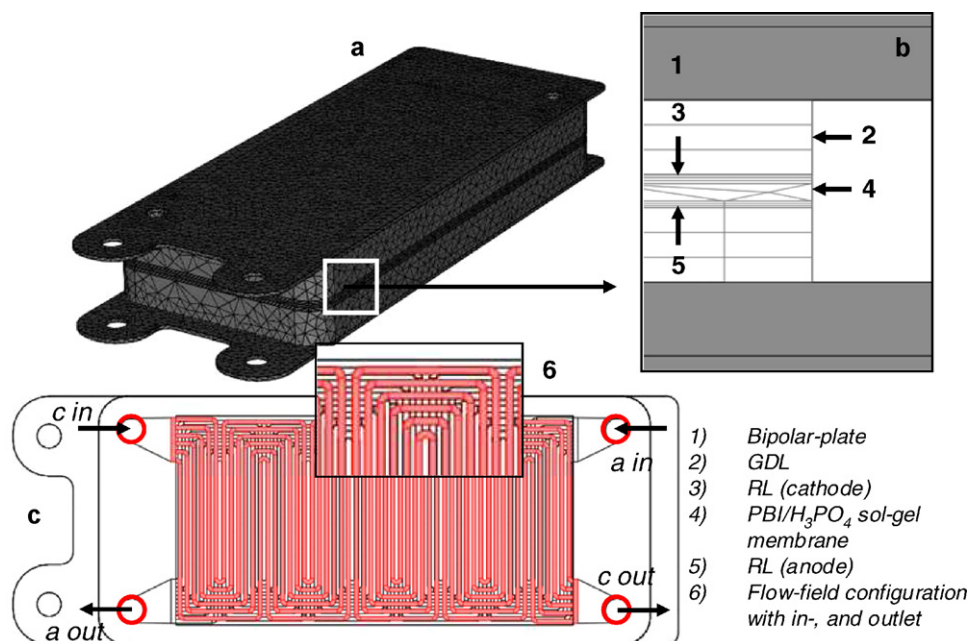

1) Bipolar-plate
2) GDL
3) RL (cathode)
4) PBI/H_3PO_4 sol-gel membrane
5) RL (anode)
6) Flow-field configuration with in-, and outlet

Fig. 3. (a) Generated 3D computational mesh in x–y–z-plane; (b) mesh details in y–z-plane; (c) gas flow channel details (180° turned against each other).

Table 4
Details recorded while solving the HTPEMFC model (base case operating conditions/20 A load current).

| Variables (DOF)	Solver settings	Iterations	Memory/GB	Clock time/s	Convergence
u_c, P_c, $Pinl\_chns_c$ (2340478)	PARDISO	16	50.4	19064	1×10^{-5}
u_a, P_a, $Pinl\_chns_a$ (2341345)	PARDISO	6	51.3	7005	1×10^{-5}
ϕ_i, ω_i (4622790)	Segregated group solver/GMRES and PARDISO	7/210	38.6	9516	1×10^{-6}
T_s, T_f (3361273)	Segregated group solver/GMRES and PARDISO	4/36	17.6	2731	1×10^{-4}

ture distributions in an iterative fashion. Table 4 lists the details recorded while solving the model for base case operating conditions. It was observed that, for such large models, the system matrix factorization generally takes longer than the solution process itself. Moreover, the number of iterations and calculation time required to meet the convergence criteria mainly depended on the cell operating voltages. The time required for calculating a typical I–V curve was roughly 48 h of clock time.

5. Results and discussion

5.1. HTPEMFC overall performance

Fig. 4 displays the simulated HTPEMFC overall performance in terms of the polarization curve at the base case operating conditions found in Table 3. The curve shows typical HTPEMFC behavior. The theoretical open circuit potential is much higher than the measured one (0.168 V about the measured value), possibly due to gas crossover and/or material imperfections. At high cell voltages, a sharp voltage drop due to activation losses (kinetics) is observed. In contrast, the voltage drop is quite low (0.031 V per 5 A) in the ohmic region. At a typical cell current of 20 A (160 °C), the cell voltage is 0.5957 V. At different operating temperatures, the cell returned 0.5724 V (140 °C) and 0.6164 V (180 °C). For a 20 A load current, the power density is 2382 W m^{-2} (160 °C), 2465 W m^{-2} (180 °C), and 2289 W m^{-2} (140 °C), respectively. The HTPEMFC model performed better at higher operating temperatures and worse at lower operating temperatures. This is consistent with the observations made during all experimental investigations.

The different contributions to the total HTPEMFC resistance are discussed in [34]. The total ohmic voltage loss (from the gold-plated copper current collector to RL) is calculated to be 20.435 mV for a 20 A load current. Under base case operating conditions and a 20 A load current, the mean overpotential at the anode- and cathode-sides was calculated to be 0.001 V and −0.485 V, respectively.
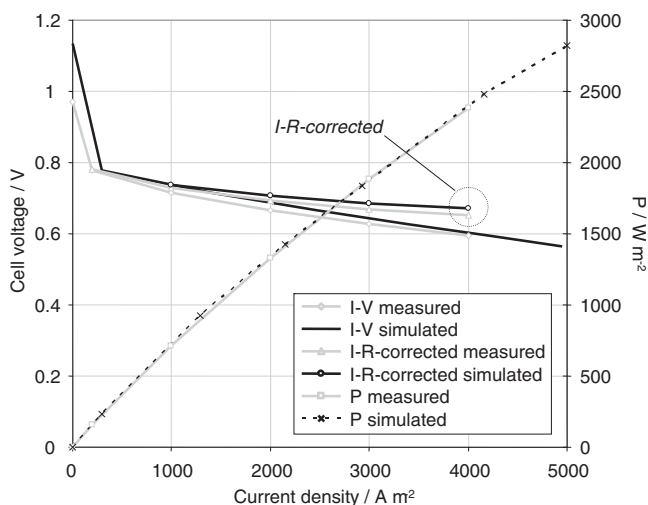
The developed model was not able to return the measured I–V curve exactly and tended to slightly overpredict the cell performance for low current densities, though good agreement is found for higher load currents. The calculated cathode-side exchange current density (Eqs. (14) and (15)) was tuned with a constant in such a way that the model returned approximately 4000 A m^{-2} at a typical cell voltage of 0.6 V. This tuned value was not changed further for other cell operating voltages or operating conditions. This indicates that the real cathode-side exchange current density may be higher than the value calculated with Eqs. (14) and (15).

5.2. Velocity and pressure distribution

Momentum transport is calculated in the gas flow channels and within the porous media. Hydrogen and air (oxygen) streams through the gas flow channels and diffuses through the void volume of the GDL and reaches the RL. Additionally, the gases have to diffuse into the electrolyte, as explained above. At stoichiometric flow rates for a 20 A load current, the mean gas flow channel velocity was calculated to be 2.1584 m s^{-1} at the cathode side and 0.4914 m s^{-1} at the anode side. For all operating conditions under consideration, the mean velocity is much lower at the anode side than on the cathode side. Because of the total flow rates, the mean velocity increases linearly when drawing more power from the cell. Moreover, the velocity towards the outlet slightly increases as oxygen is consumed and water is produced, but no significant change in velocity was observed within the anode-side gas flow channel.

Within the porous media, the mean velocity values were calculated to be several orders of magnitude lower than those in the gas flow channels (e.g., 0.001916 m s^{-1} within the cathode-side porous media at stoichiometric flow rates for a 20 A load current). Fig. 5 depicts the local gas velocities within the middle of the GDL.

When taking a closer look at the velocity distribution within the porous media, it is seen that much higher velocity values are

Fig. 4. Measured and simulated HTPEM fuel cell performance at base case operating conditions.
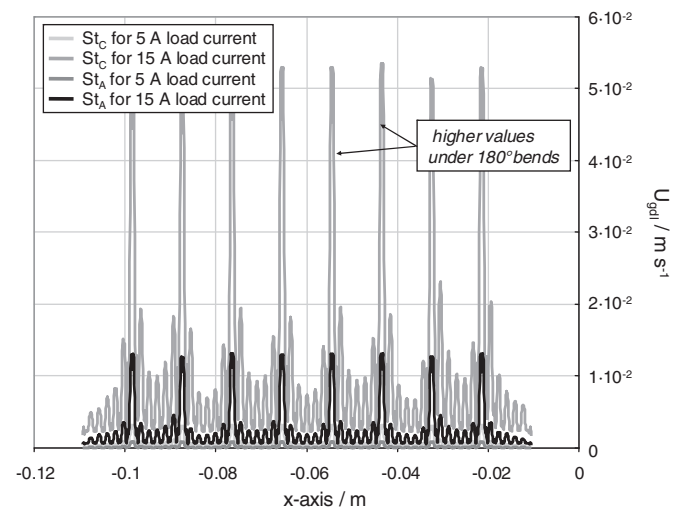
Fig. 5. Local anode- and cathode-side GDL velocity along the x-axis ($y/y_{max} = 1/2$, $z = -150 \times 10^{-6}$ m) at different stoichiometric flow rates without drawing current from the cell.
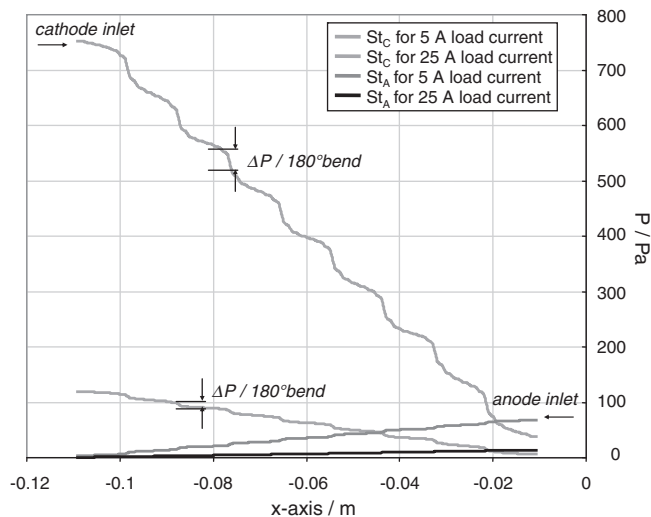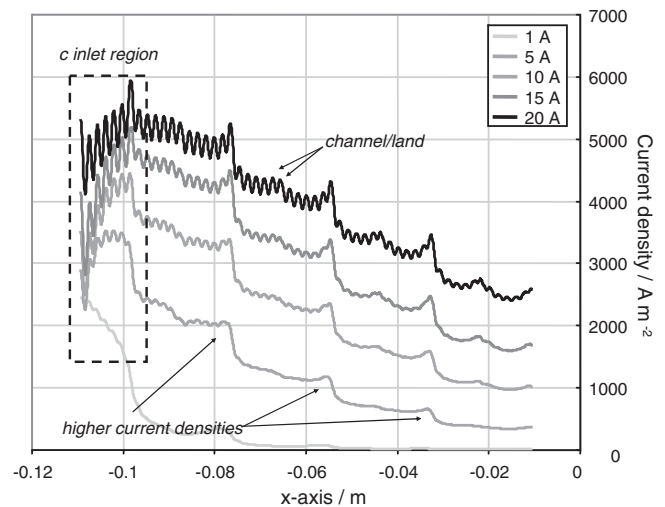
Fig. 6. Local anode and cathode-side GDL pressure loss along the x-axis ($y/y_{max} = 1/2$, $z = -150 \times 10^{-6}$ m) at different stoichiometric flow rates without drawing current from the cell.

Fig. 8. Cathode-side RL current density distribution in along the x-axis (plot A–A′, $z = -379 \times 10^{-6}$ m) at base case operating conditions for 5 A, 10 A, 15 A, 20 A, and 25 A load currents.

observed in the region under each 180° bend. This is due to the fact that a pressure difference (e.g., 50 Pa at a 15 A load current) exists at the same locations, as can be seen in Fig. 6. Consequently, a certain amount of gas bypasses the gas flow channels through the porous media (a.k.a. cross-leakage flow). This effect may lead to a higher concentration of the reactants in the regions close to the RL and might be a reason for higher current density values at these locations (see Figs. 7 and 8).

For a 25 A load current, the net pressure loss was 700 Pa over the cathode gas flow channel and 80 Pa over the anode gas flow channel. These pressure losses are low compared to similar LTPEMFC operating conditions; nevertheless, it must be noted that although the reported values are the net pressure losses over the exact length of the flow-field. The simulated values are lower than the measured ones because this HTPEMFC model does not account for any additional peripheral pressure losses. For the same load current (25 A), the measured pressure loss was 2400 Pa at the cathode side and 250 Pa at the anode side. In fact, the presence of the gas connectors, the gas pipes towards the differential pressure transmitters, the in-, and outlet manifold, as well as the gas distributor lead to higher pressure losses as gas recirculation zones, expansion zones (e.g. sudden expansion), and/or contraction zones may exist. Results elucidate that a detailed modeling of the entire gas piping system

would give a clearer picture of absolute pressure values. Overall, qualitative results were in agreement with the particle image velocimetry (PIV) measurements presented in [32].

5.3. Current density distribution

Fig. 7 shows the current density distribution at the MEA surface (RL) for a cell operated at base case operating conditions at 5 A, 10 A, 15 A, 20 A, and 25 A load currents (left to right). All five operating conditions have similar current density distributions with higher values towards the air inlet and lower values towards the air outlet. Oxygen decreases almost linearly along the gas flow channel and towards the RL due to electrochemical reactions. The distribution of the oxygen mass fraction dominates the current density distribution. Additionally, the distribution is strongly influenced by the bipolar plate or flow-field structure. At the exit of the cathode gas flow channel, the O_2 mole fraction is calculated to be 0.15 for the given cathode stoichiometries and inlet mole fractions. It is clear that no water flooding occurs within the porous media, and the water vapor mass fraction increases towards the cathode-side outlet (oxygen dilution). Higher values are observed under the land areas and close to the borders of the MEA, especially towards the cathode outlet region. This is reasonable because the water
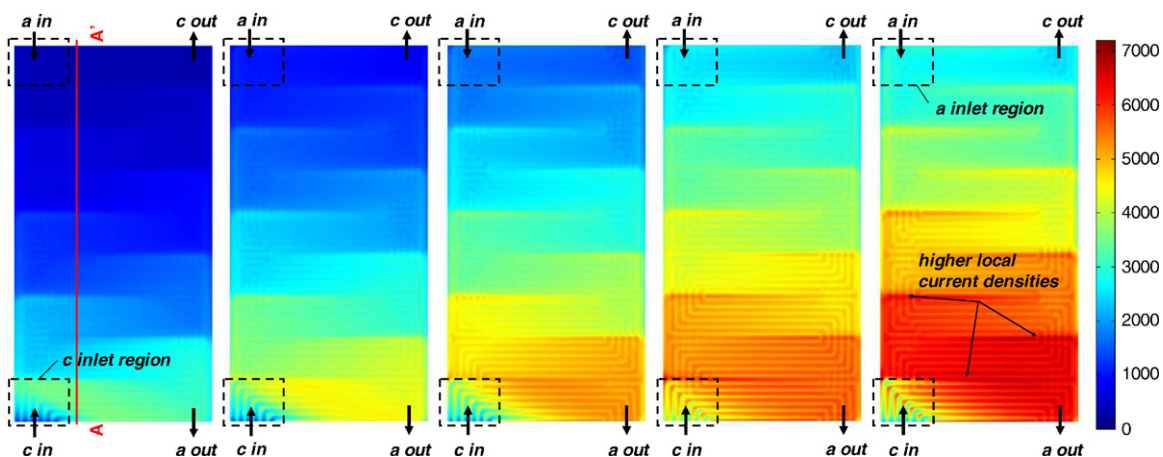
Fig. 7. Cathode-side RL current density distribution in the x–y-plane ($z = -379 \times 10^{-6}$ m) at base case operating conditions for 5 A, 10 A, 15 A, 20 A, and 25 A load currents (left to right).

Table 5
Mean solid-phase temperature within the HTPEMFC components / °C.

	1 A	5 A	10 A	15 A	20 A	25 A
Anode side						
Cu	160.07	160.19	160.329	160.442	160.556	160.64
BPP	160.04	160.193	160.35	160.491	160.614	160.73
GDL	160.02	160.5	161.02	161.47	161.91	162.25
RL	160.06	160.69	161.39	161.99	162.58	163.03
MEM	160.079	160.75	161.48	162.126	162.75	163.22
Cathode side						
RL	160.08	160.791	161.55	162.226	162.87	163.41
GDL	160.055	160.57	161.13	161.63	162.11	162.47
BPP	160.04	160.626	160.78	160.924	161.048	161.16
Cu	160.07	160.623	160.76	160.87	160.99	161.07

vapor has to diffuse through the porous media towards the gas flow channel before it leaves the cell.

In addition to the oxygen mass fraction, the current density is influenced by the fluid-phase (and/or solid-phase) temperature as cold gases enter the cell (compare with Figs. 9 and 10). It can be seen that the influence is more significant at higher currents due to larger total gas-flow rates. This effect is even noticed in the region of the anode inlet for higher load currents. Over the entire MEA area, higher current density values are observed under the ribs than under the channels of the bipolar plate. The maximum current density values are seen in the regions where the 180° bends are located. This may be caused by higher local velocity and reactant concentration values within the RL, as discussed above and mentioned in [23,32].

Fig. 8 provides fine details about the current density distribution along the x-axis and highlights the above-mentioned aspects. Close to the cathode inlet, the current density under the land is much higher than under the channel. Moreover, the observed variations become less pronounced towards the cathode outlet for all load currents. The individual current density peaks at each 180° bend can clearly be seen. The above results indicate that the channel-to-land ratio should be seen as an optimization parameter for the flow-field layout used for HTPEMFC, especially at the cathode side.

As for the anode side, it was observed that the distribution of the hydrogen mass/mole fraction is much smoother, having higher values in the gas flow channels than in the porous media (consumption in z-direction towards the RL). The influence of the BPP structure can hardly be seen. It is expected that hydrogen easily reaches the catalysts, where it is finally consumed. At the exit of the anode gas-flow channel, the H_2 mole fraction is calculated to be 0.985 for the given anode stoichiometries and inlet mole fractions. This variation is small due to the low molar mass of H_2 and, because no water is produced at the anode side. Additionally, it is assumed that no water is transferred from the cathode to the anode side via the membrane or water absorbed by the membrane.

5.4. Solid-phase temperature distribution

The solid-phase temperature within the gold-plated copper current collectors and both BPPs seems to be almost uniform due to the high thermal conductivities of both materials compared to all other thermal conductivities within the setup. Only slightly higher solid-phase temperatures are observed within these components when drawing higher load currents. Table 5 lists the calculated values for the anode- and cathode-side components. The mean RL solid-phase temperature rise at 25 A load current at the cathode side is 3.41 °C and 2.87 °C at 20 A, compared to no load operating conditions (set to 160 °C). It is expected that this rise in temperature will be much more pronounced at load currents of 30–40 A, since much more head will produced. Anyways, these operating points are not explicitly discussed in this work.

Within the porous media, the solid-phase temperature is strongly influenced by the cold gases entering the cell (Fig. 9). This fact is observed at both gas inlets. At the anode side, even though the total gas flow is lower, the effect is much more pronounced in terms of temperature than on the cathode side. On the other hand, a much larger MEA area is influenced on the cathode side. The maximum solid-phase temperature is observed close to the region where the highest current density is also located (164 °C at a 20 A load current and 165 °C at a 25 A load current). When taking a closer look at the solid-phase temperature distribution, it is seen that the shape of both flow-fields influences its distribution. The temperature in the regions under the gas-flow channels is somewhat lower. This temperature difference almost vanishes towards the exit. For base case operating conditions and a 20 A load current, the total amount of heat produced is calculated to be 11.22 W. Most of the heat is produced within the cathode-side RL (10.61 W). Of this value, the irreversible reaction heat comprises 69%, the reaction entropy comprises 30%, and the total joule heating (resistive heating) makes up the remaining 1%.

A major drawback of this model setup is the fact that a constant temperature is defined at both copper current collector boundaries. In fact, much higher temperatures are expected within the endplates (up to 180–200 °C in the region close to the heating elements) because, in most single cell setups, heating elements are used to keep the HTPEMFC at operating temperature.

5.5. Fluid-(gas)-phase temperature distribution

The gases are heated as they diffuse through the porous media (in the z-direction towards the RL). The fluid-(gas)-phase temperature distribution for different load currents within the cathode-side RL is given in Fig. 10. Again, when drawing more current, more gas enters the cell. Consequently, it takes longer until the gas reaches the cell operating temperature. More heat needs to be exchanged between the two phases, and the thermal equilibrium between the solid-, and the fluid-(gas)-phases shifts in the direction of the channel. Within the anode-side porous media, 0.448 W are transferred, whereas 1.619 W are transferred between the two phases at the cathode-side.

Fig. 11 shows the anode and cathode-side fluid-(gas)-phase temperature behavior within the middle of the gas flow channel. At the anode side, hydrogen heats up very quickly (high thermal conductivity and a high heat capacity) and reaches cell operating temperature shortly after entering the gas flow channels. At the cathode side, it takes much longer for the gas mixture to reach thermal phase equilibrium. Both, Fig. 11 ($z = 500 \times 10^{-6}$ m) and Fig. 10 ($z = -379 \times 10^{-6}$ m) show the same trend when it comes to fluid-phase temperature distribution. The difference is that it takes slightly longer until phase equilibrium is reaches within the gas flow channels (higher convection) than within the porous media. This behavior was observed for all load currents.

The heat flux vectors within the high magnification image in Fig. 11 depict the solid-to-fluid heat transfer via the gas flow channel (bipolar plate) walls (using a constant heat transfer coefficient at these boundaries). It can be seen that the gas temperature is becomes slightly higher close to the bipolar plate (gas flow channel) boundaries. For base case operating conditions and a 20 A load current, 0.0146 W and 1.0747 W are transferred through these walls at the anode and cathode side, respectively.

5.6. Membrane conductivity

Eqs. (11)–(13) satisfactorily describe the overall membrane conductivity only in a small temperature range around 160 °C. For higher temperatures, e.g., $T_s > 170$ °C, the calculated conductivities do not match the measured data in [34], indicating that, in
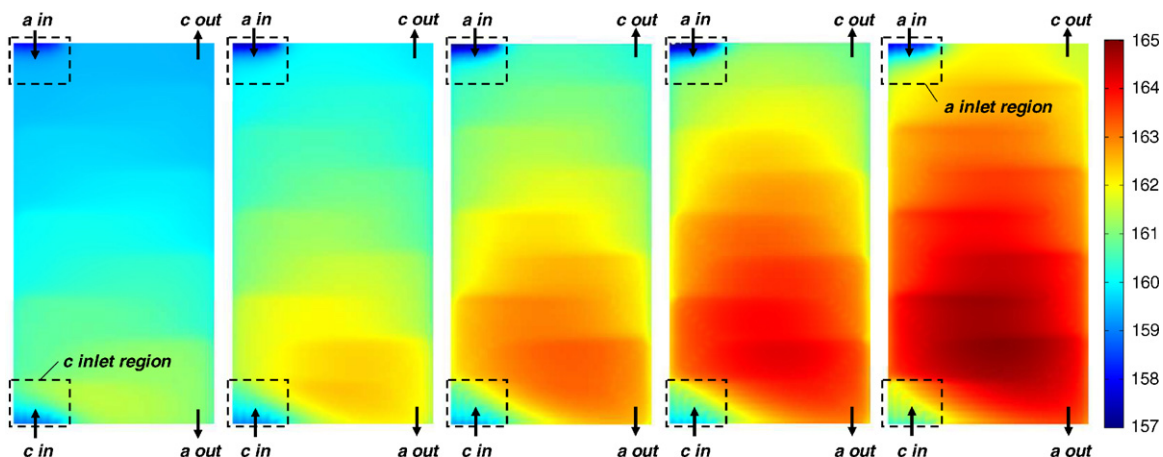
Fig. 9. Cathode-side RL solid-phase temperature distribution in x–y-plane ($z = -379 \times 10^{-6}$ m) at base case operating conditions for 5 A, 10 A, 15 A, 20 A, and 25 A load current (left to right).
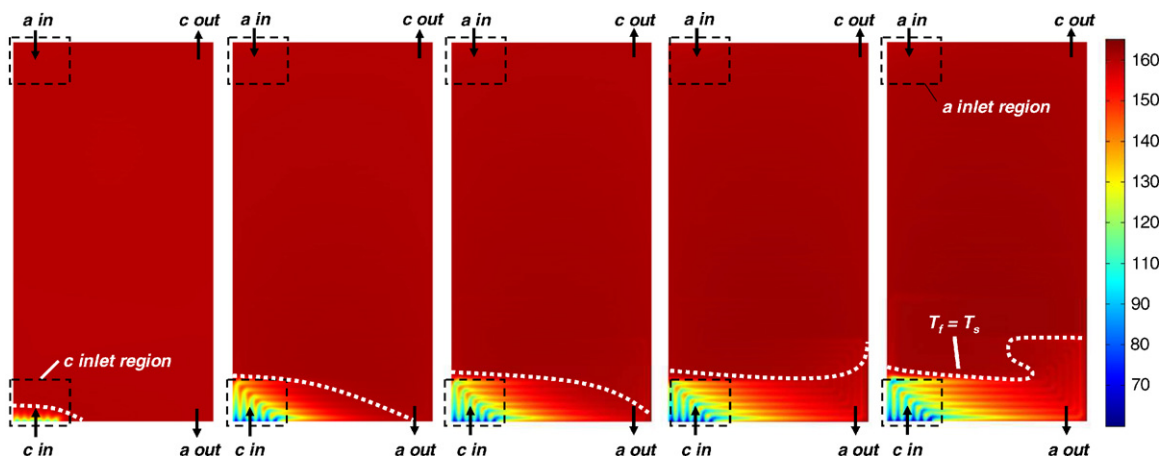

Fig. 10. Cathode-side RL fluid-(gas)-phase temperature distribution in x–y-plane ($z = -379 \times 10^{-6}$ m) at base case operating conditions for 5 A, 10 A, 15 A, 20 , and 25 A load currents (left to right).

this range of temperatures, other mechanisms of proton conduction may be present and may be influenced by the concentration changes of the acid within the PBI/H$_3$PO$_4$ system. Though the conductivity values of the PBI/H$_3$PO$_4$ sol–gel membranes are quite

high, the values are still lower than the reported values for hot concentrated H$_3$PO$_4$ by a factor of approximately three (160 °C). This indicates that the transport process through this type of membrane is not as continuous as in hot concentrated H$_3$PO$_4$, which is
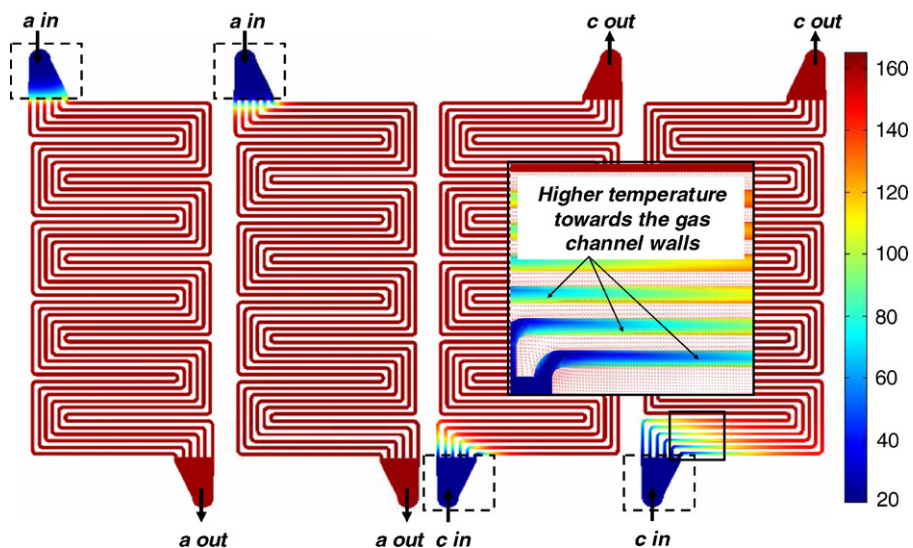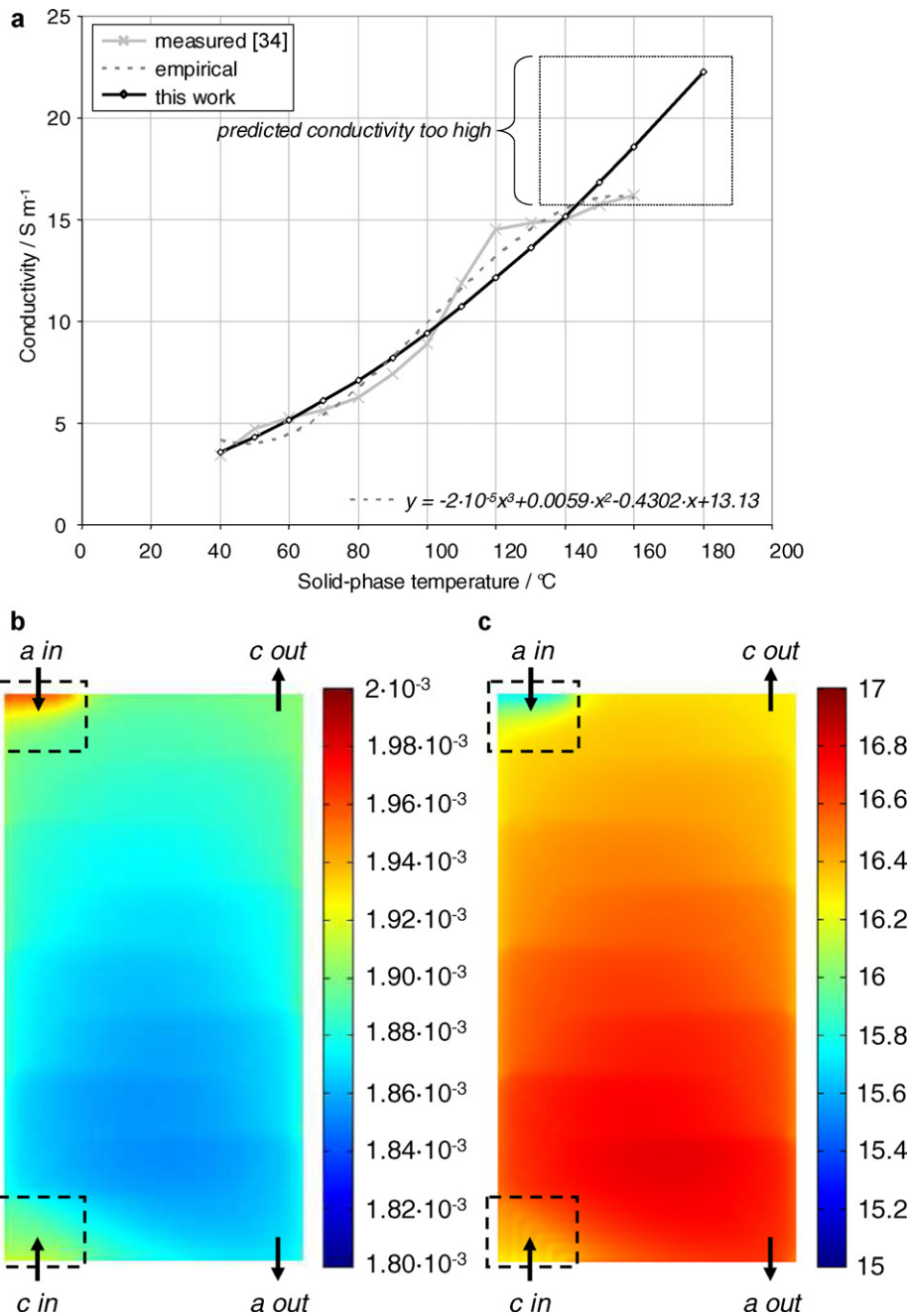

Fig. 11. Fluid-(gas)-phase temperature distribution within the anode- and cathode-side gas flow channels ($z = 500 \times 10^{-6}$ m) at base case operating conditions in the x–y-plane for 5 A (anode-side), 20 A (anode-side), 5 A (cathode-side), and 20 A (cathode-side) load currents (left to right).

Fig. 12. (a) Membrane conductivity at various solid-phase temperatures; (b) membrane resistance distribution in the x–y-plane ($z = -430 \times 10^{-6}$ m) for base case operating conditions at a 20 A load current; (c) membrane conductivity distribution in the x–y-plane ($z = -430 \times 10^{-6}$ m) for base case operating conditions at a 20 A load current.

consistent with other types of high-temperature stable membranes [7].

This model assumes no gas crossover or water transfer through the membrane. In Eq. (12), the pre-exponential factor and the activation energy are taken to be constant. Consequently, the local membrane conductivity distribution follows the solid-phase temperature distribution. The minimum ($15.7\,\mathrm{S\,m^{-1}}$) is close to the anode-side inlet, whereas the maximum ($17\,\mathrm{S\,m^{-1}}$) is located in the lower third of the MEA, as can be seen from Fig. 12.

The membrane resistance calculated from the model was $1.877\,\mathrm{m\Omega}$, which is in good agreement with the measured value. Again, its distribution follows the membrane conductivity distribution. At base case operating conditions and a 20 A load current, the voltage loss over the membrane was 0.03927 V.

5.7. Changes in H_3PO_4 during cell operation

This model assumes no water through or water uptake by the membrane (see assumption 6). It uses a simple approach to couple the partial pressure of water to the phosphoric acid concentration and temperature within both RL, as seen in Eq. (25). The calculated H_3PO_4 (and amorphous phase H_3PO_4) concentration changes for different load currents because more water is produced. At the anode side, the partial pressure of water remains more or less constant, whereas it increases towards the exit at the cathode side. The model results indicate that the H_3PO_4 concentration is reduced for higher water vapor partial pressures. For base case operating conditions, it is observed that the H_3PO_4 concentration reaches much higher values than the initially assumed concentration of 85 wt.%
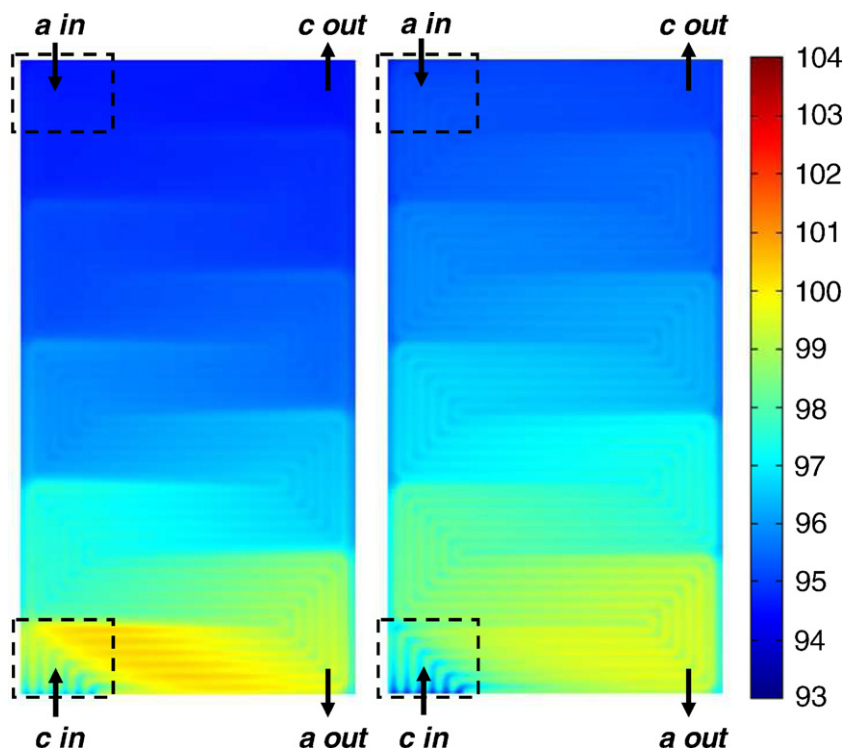
Fig. 13. Phosphoric acid concentration distribution in the x–y-plane ($z = -379 \times 10^{-6}$ m) for base case operating conditions at 5 A (left) and 20 A load currents (right).

at RTP, as can be seen in Fig. 13. At the anode and cathode side, the mean concentrations are calculated to be 100.23% and 96.79%, respectively (based on molecular H_3PO_4). The mean partial pressure of water is calculated to be 1802 Pa at the anode-side and 18134 Pa at the cathode-side RL (base case operating conditions and a 20 A load current). Moreover, from Fig. 13 it can be seen that the highest values at the cathode side are located close to the inlet in the lower third over the MEA. Locally, lower values are seen under the land areas because more water vapor is present. It must be noted that the reported concentration values may change when accounting for water adsorption and desorption in PBI/H_3PO_4 systems.

The H_3PO_4 concentration values and the temperature influence the gas diffusivity and gas solubility in amorphous phase H_3PO_4. For base case operating conditions, slightly lower air diffusivity values were located close to the cathode inlet, whereas almost constant values were observed over the remaining MEA area. All calculated diffusivity values were in good agreement with the values reported for hot concentrated H_3PO_4.

The air solubility had the same characteristic distribution as the phosphoric acid concentration in Fig. 13. For base case operating conditions and a 20 A load current, the solubility ranged from 0.504 to 0.529 mol m^{-3} atm^{-1}. This means that both the gas diffusivity and the solubility are somewhat lower close to the cathode inlet, influencing the local current density values.

Nevertheless, much more experimental and theoretical work (e.g., molecular dynamics simulations) is necessary to precisely identify the interactions of H_3PO_4, PBI, and water vapor to develop an adequate phosphoric acid transport model for continuous operation and start/stop cycling.

6. Conclusion

A complete non-isothermal three-dimensional model of a HTPEMFC setup using a PBI/H_3PO_4 sol–gel membrane was developed, modeled, and solved using COMSOL Multiphysics®. Additional equations were directly coded into the FEM/CFD software using scalar, boundary, and subdomain expressions. Computational aspects are listed in order to paint a clear picture of the soft-, and hardware requirements when solving large scale models using finite elements. Electrochemical reactions were described using an agglomerate approach that considered the diffusivity and solubility of the gases. The model was able to reproduce the achieved experimental results for 0–20 A load currents. The membrane conductivity was modeled using an Arrhenius approach that seems to be valid for solid-phase temperatures up to 150–160 °C. For higher temperatures, this approach may overpredict the membrane conductivity since the amorphous phase H_3PO_4 concentration changes may influence the proton conduction mechanisms. Results also show how the H_3PO_4 concentration is influenced during cell operation. Beside, the model setup is able to simulate the dependency of the current density distribution on the fluid-flow distribution and on the solid- and fluid-(gas)-phase temperature distribution in a HTPEMFC. Highest solid-phase temperature is observed in the region of the highest current density. Moreover, it highlights the interaction between the two temperatures, including localized cooling effects close to the gas inlets by reporting values for the amount of transferred heat. Consequently, the fluid-(gas)-phase inlet temperature and the gas manifold and flow-field design should be seen as an important factor for optimal operation, especially when designing gas manifolds and gas-inlet sections for larger HTPEMFC stacks. This general-purpose model may be useful when analyzing HTPEMFC operational behavior because it exemplifies the complex couplings between all transport equations and electrochemical reactions. Based on the results, it is now possible to optimize the flow-field structure and minimize current density distribution gradients over the MEA. It will be the basis of future HTPEMFC modeling activities that may include possible water transfer through the PBI/H_3PO_4 system, gas crossover and an ameliorated H_3PO_4 transport model.

Acknowledgements

References

[1] J.S. Wainright, J.-T. Wang, D. Weng, R.F. Savinell, M. Litt, J. Electrochem. Soc. 142 (1995) L121–L123.
[2] S.R. Samms, S. Wasmus, R.F. Savinell, J. Electrochem. Soc. 143 (1996) 1225–1232.
[3] J.-T. Wang, R.F. Savinell, J.S. Wainright, M. Litt, H. Yu, Electrochim. Acta 41 (1996) 193–197.
[4] Th. Dippel, K.D. Kreuer, J.C. Lassègues, D. Rodriguez, Solid State Ionics 61 (1993) 41–46.
[5] R. Bouchet, E. Siebert, Solid State Ionics 118 (1999) 287–299.
[6] Q. Li, R. He, R.W. Berg, H.A. Hjuler, N.J. Bjerrum, Solid State Ionics 168 (2004) 177–185.
[7] Y. Ma, The Fundamental Studies of Polybenzimidazole/Phosphoric Acid Polymer Electrolyte for Fuel Cells, Dissertation, Case Western Reserve University, 2004.
[8] L. Xiao, H. Zhang, E. Scanlon, S. Ramanathan, E.-W. Choe, D. Rogers, T. Apple, B.C. Benicewicz, Chem. Mater. 17 (2005) 5328–5333.
[9] T.J. Schmidt, ECS Trans. 1 (2006) 19–31.
[10] T.J. Schmidt, J. Baurmeister, J. Power Sources 176 (2008) 428–434.
[11] N.H. Jalani, M. Ramani, K. Ohlsson, S. Buelte, G. Pacifico, R. Pollard, R. Staudt, R. Datta, J. Power Sources 160 (2006) 1096–1103.
[12] J. Zhang, Y. Tang, C. Song, J. Zhang, J. Power Sources 172 (2007) 163–171.
[13] J. Zhang, Z. Xie, J. Zhang, Y. Tang, C. Song, T. Navessin, Z. Shi, D. Song, H. Wang, D.P. Wilkinson, Z.-S. Liu, S. Holdcroft, J. Power Sources 160 (2006) 872–891.
[14] Q. Li, J.O. Jensen, R.F. Savinell, N.J. Bjerrum, Prog. Polym. Sci. 34 (2009) 449–477.
[15] D. Cheddie, N. Munroe, J. Power Sources 156 (2006) 414–423.
[16] D. Cheddie, N. Munroe, J. Power Sources 160 (2006) 215–223.
[17] D. Cheddie, N. Munroe, Energy Convers. Manage. 47 (2006) 1490–1504.
[18] D. Cheddie, N. Munroe, Int. J. Hydrogen Energy 32 (2007) 832–841.
[19] J. Peng, S.J. Lee, J. Power Sources 162 (2006) 1182–1191.
[20] J. Peng, S.J. Lee, J. Power Sources 179 (2008) 220–231.
[21] K. Scott, S. Pilditch, M. Mamlouk, J. Appl. Electrochem. 37 (2007) 1245–1259.
[22] E.U. Ubong, Z. Shi, X. Wang, ECS Trans. 16 (2008) 79–90.
[23] B. Schaar, Simulation einer Hochtemperatur-PEM-Brennstoffzelle, AutoUni-Schriftreihe, Dissertation, Logos Verlag Berlin, Berlin, 2008.
[24] O. Shamardina, A. Chertovich, A.A. Kulikovsky, A.R. Khokhlov, Int. J. Hydrogen Energy (2009), doi:10.1016/j.ijhydene.2009.11.012.
[25] A.A. Kulikovsky, H.-F. Oetjen, Ch. Wannek, Fuel Cells. doi:10.1002/fuce.200900135.
[26] T. Sousa, M. Mamlouk, K. Scott, Chem. Eng. Sci (2010), doi:10.1016/j.ces.2009.12.038.
[27] F. Zenith, F. Seland, O.E. Kongstein, B. Børresen, R. Tunold, S. Skogestad, J. Power Sources 162 (2006) 215–227.
[28] C.-P. Wang, H.-S. Chu, Y.-Y. Yan, K.-L. Hsueh, J. Power Sources 170 (2007) 235–241.
[29] A. Bergmann, D. Gerteisen, T. Kurz, Fuel Cells. doi:10.1002/fuce.200900128.
[30] C. Siegel, G. Bandlamudi, A. Heinzel, Proceedings of the European COMSOL Conference, Grenoble, France, 2007.
[31] C. Siegel, G. Bandlamudi, A. Heinzel, Proceedings of the European COMSOL Conference, Hannover, Germany, 2008.
[32] C. Siegel, G. Bandlamudi, A. Heinzel, Proceedings of the European COMSOL Conference, Milan, Italy, 2009.
[33] C. Siegel, G. Bandlamudi, A. Heinzel, Proceedings of the Fuel Cell Science & Technology Conference, Copenhagen, Denmark, 2008.
[34] G. Bandlamudi, C. Siegel, A. Heinzel, J. Power Sources, submitted for publication.
[35] J.J. Hwang, J. Electrochem. Soc. 153 (2006) A216–A224.
[36] S.R. Choudhury, M.B. Deshmukh, R. Rengaswamy, J. Power Sources 112 (2002) 137–152.
[37] COMSOL Multiphysics® v3.5a 2010. http://www.comsol.com.
[38] K. Broka, Characterization of the Components of the Proton Exchange Membrane Fuel Cell, Techn. Lic. Thesis, Royal Institute of Technology Stockholm, 1995.
[39] R.B. Bird, W.E. Stewart, E.N. Lightfoot, Transport Phenomena, John Wiley & Sons Inc., New York, 1960.
[40] Z. Liu, J.S. Wainright, M.H. Litt, R.F. Savinell, Electrochim. Acta 51 (2006) 3914–3923.
[41] J.C. Huang, R.K. Sen, E. Yeager, J. Electrochem. Soc. 126 (1979) 786–792.
[42] D.I. MacDonald, J.R. Boyack, Chem. Eng. Data 14 (1969) 380–384.
[43] M.S. Gallart, Computational modeling and optimization of proton exchange membrane fuel cells, Dissertation, University of Victoria, 2007.
[44] K. Klinedinst, J.A.S. Bett, J. MacDonald, P. Stonehart, J. Electroanal. Chem. Interfacial Electrochem. 57 (1974) 281–289.
[45] E-tek ELAT® 2009. http://www.etek-inc.com.
[46] R.M. Rao, D. Bhattacharyya, R. Rengaswamy, S.R. Choudhury, J. Power Sources 173 (2007) 375–393.
[47] A.G. Turnbull, J. Chem. Eng. Data 10 (1965) 118–119.
[48] C. Siegel, Energy 33 (2008) 1331–1352.